Ultramafic Melt Viscosity: A Model

James K. Russell[1], Kai-Uwe Hess[2], and Donald B. Dingwell[2]

Earth and Planetary Science Letters

Submitted May 13, 2024

Accepted July 14, 2024

[1]Volcanology and Petrology Laboratory, Department of Earth and Ocean Sciences, University of British Columbia, Vancouver, British Columbia, V6T 1Z4, Canada

[2]Department für Geo- und Umweltwissenschaften, Ludwig-Maximilians-Universtät München, 80333 Munich, Germany

Corresponding Author: J.K. Russell (krussell@eoas.ubc.ca)

ABSTRACT

A non-Arrhenian model for the Newtonian viscosity (η) of ultramafic melts is presented. The model predicts the viscosity of ultramafic melts as a function of temperature (*T*), pressure (*P*), H_2O content and for a range of melt compositions ($70 < Mg\# < 100$). The calibration consists of 63 viscosity measurements at ambient pressure for 20 individual melt compositions and 5 high-P measurements on a single melt composition, all drawn from the literature. The data span 14 orders of magnitude of η (10^{-2} to $10^{11.8}$ Pa s), a T range of 880 to 2700K, pressures from 1 atm to 25 GPa, and include measurements on hydrous melts containing 0.2 to 4.4 wt. % H_2O. The T-dependence of viscosity is modelled with the VFT equation [$\log \eta = A + B/(T(K) - C)$] whereby *A* is assumed to be a common, high-T limit for these melt compositions (*i.e.* $\log \eta_\infty = -5.4$). The pressure and composition effects are parameterised in terms of 5 adjustable parameters in expanded forms of *B* and *C*. The viscosity model is continuous across *T*-*P*-composition space and can predict ancillary transport properties including glass transition temperatures (*Tg*) and melt fragility (*m*). Melt viscosity decreases markedly with increasing H_2O content but increases significantly with increasing pressure and decreasing *Mg#* (i.e. higher Fe-content). We show strong systematic decreases in *Tg* and *m* with increasing H_2O content whereas an increase in *P* causes a rise in *Tg* and decrease in *m*. The predictive capacity of this model for ultramafic melt viscosity makes it pertinent to the fields of volcanology, geophysics, petrology, and the material sciences. Moreover, it provides constraints on models of magma oceans on terrestrial planets and, the evolution of planetary atmospheres via magmatic degassing on exoplanets.

Keywords: Viscosity, Melts, Ultramafic, Peridotite, Pyrolite, Komatiite, Model, Temperature, Pressure, Volcanic, Magmatic, Magma Ocean

1. Introduction

Terrestrial magmatism and volcanism have involved ultramafic silicate melts throughout earth history, via the generation of komatiite, kimberlite, and other less common alkaline melts (e.g., Arndt, 2003). Primordial Earth is believed to have been host to a deep, mafic to ultramafic, magma ocean that facilitated core formation and early differentiation and crystallization of Earth's interior (e.g. Fiquet et al., 2010; de Vries et al., 2016; Sun et al., 2020; Bajgain et al., 2022). Reasonable estimates of the processes controlling the accumulation and differentiation of terrestrial planets, including 1000s of newly discovered exoplanets, suggest the near-ubiquitous presence of ultramafic melts at some stage in the geological history of planets (Putirka and Xu, 2021).

Despite the crucial role they play in planetary differentiation and degassing, ultramafic melts are under-investigated relative to other terrestrial silicate melts (cf. Xie et al., 2021; Russell et al., 2022). The viscosity of ultramafic melts, as a function of temperature (T), pressure (P), and water content (X_{H2O}), is, as a result, poorly constrained (DiGenova et al., 2023; See Supplement). The prediction of viscosity for ultramafic melts at terrestrial P-T-X_{H2O} conditions is an important component to modelling 1) timescales of crystallization and degassing of magma oceans (e.g., Bajgain et al., 2022), 2) fragmentation conditions driving explosive eruption of low viscosity magmas (Moss et al., 2011; Jones et al., 2022), and 3) the efficiency of differentiation processes (e.g., convection and cooling) in lithosphere-hosted magma reservoirs.

Here, we have compiled and employed the available experimental data to develop a predictive model for the temperature(T)-pressure(P)-composition(X) dependence of viscosity for anhydrous and hydrous ultramafic melts. The model reproduces the original data (T ~880-2800K; $P \leq 25$ GPa) to within experimental error and predicts the rheological behaviour of ultramafic melts, including the glass transition temperature (*Tg*) and melt fragility (*m*), as a function of magnesium number (i.e. *Mg#*) and H_2O content, temperatures, and pressures up to 160 GPa. The model provides a robust means of exploring volcanic, magmatic and mantle processes involving anhydrous and hydrous ultramafic melts including pyrolite, peridotite, and komatiite.

2. Data Compilation

Our compilation of viscosity measurements for ultramafic melts together with the corresponding melt compositions and their literature sources can be found as Supplementary Material. The compiled dataset includes five base melt compositions including peridotite (Dingwell et al., 2004; DiGenova et al., 2023), pyrolite (Casas et al., 2023), Fe-free and high-Ca peridotite (DiGenova et al., 2023) and oxidized or reduced equivalents. Melt compositions are reported in terms of the five major oxide components of ultramafic chemistry SiO_2-Al_2O_3-FeO-MgO-CaO (wt. %) as well as several minor oxide components (e.g. TiO_2, Na_2O, etc.). The compositional ranges of the melts used to calibrate the model include (in wt. %): SiO_2, 40-51; Al_2O_3, 3-6.6; FeO_T, 0-16; MgO, 25-41; and CaO, 2-17 and the melts have magnesium numbers (*Mg#* calculated as mol. % MgO/[MgO+FeO_T]) of 74-99 (average of 88; Fig. 1). The compilation also includes measurements on peridotite melts with four different water contents from 0.23 to 4.4 wt. % H_2O (DiGenova et al., 2023). We have restricted our experimental database to include highly depolymerized, multicomponent silicate melts whose NBO/T (Mysen et al., 1982; Mysen, 1988) range from 1.9 to 3.5 and SM (structural modifier parameter) values vary from 47 to 64 (Fig. 1D). SM indices are calculated after Giordano and Dingwell (2003) as the mol. % summation of CaO, MgO, MnO, 0.5 FeO_T, Na_2O, and K_2O.

The experimental measurements used to calibrate the viscosity model comprise a total of 68 pairs of viscosity–temperature data (Fig. 1A), including 9 made by concentric cylinder viscometry and 10 by micropenetration dilatometry. The data were directly taken from the publications, without modifications. The database also includes 44 estimates of melt viscosity made from conventional (N=37) or flash (N= 7) differential scanning calorimetry (DSC) experiments using the shift factor (SF) method (Scherer, 1984). DiGenova et al. (2023) opted to employ a chemically invariant shift factor concept (SF onset = 11.20; SF peak = 9.84), which is commonly used in the technical glass community (e.g., Al-Mukadam et al., 2020). Most commonly, those melts are relatively fragile, and one can assume a compositional independence for the shift factor as a first order approximation. However, Gottsmann et al. (2002) showed, for geological melts, a significant compositional dependence of the shift factor. Based on that work, Dingwell et al. (2004) derived a SF peak of 9.65 for peridotite melt compositions and this value was recently used successfully by Casas et al. (2023) for pyrolite melt compositions. On that basis, we have elected to use a SF peak of 9.65 and an adjusted SF onset of 11.01 to convert DSC data (i.e. *Tg* peak, *Tg* onset) from DiGenova et al.'s (2023) study of anhydrous peridotite melts to equivalent values of melt viscosity.

The hydrous samples of DiGenova et al. (2023) were synthesised at high-temperature and high-pressure (Fig. 1). However, the resulting experimental data were obtained on supercooled liquids, which had undergone relaxation at 1 atm. Those data, therefore, do not preserve information on viscosity at elevated pressure and do not inform on any potential pressure dependence of water speciation or its effect on viscosity. If water speciation is pressure dependent our pressure-dependent model (see below) would not capture its effect(s).

Lastly, the compilation includes five high-pressure measurements of anhydrous melt viscosity using *in situ* falling sphere viscometry (Xie et al., 2021). Values of melt viscosity range from $10^{-1.8}$ to $10^{11.8}$ Pa s over the temperature range of 622 to 2500°C and a pressure range of 1 atm to 25 GPa (Fig. 1A). Although our compiled dataset is comprehensive, it must be considered sparse and not extensive enough to explore all possible dependencies - such as the effects of pressure on redox or H_2O speciation. Furthermore, it must be emphasized that the pressure dependence we model is based on physical experiments performed on a single anhydrous (i.e. not hydrous) melt composition (Xie et al., 2021). Future datasets will provide a means to, both test and refine, our model.

3. Model Development

We have elected to use the Vogel-Fulcher-Tammann (VFT, Eq. 1) function:

$$log\,\eta = A + \frac{B}{T - C} \qquad (1)$$

to account for the T-dependence of viscosity of the silicate melts (Fulcher, 1925). The VFT function fits viscosity data well over large ranges of temperature and composition, is purely empirical, and has only three adjustable parameters (e.g., Richet, 1984; Russell et al., 2003; 2022).

Based on the compiled measurements of viscosity, the largest effect on viscosity, after temperature, is dissolved H_2O content which, as observed for most silicate melts, decreases melt viscosity by up to 4 orders of magnitude (e.g., Hess and Dingwell, 1996; Schulze et al., 1996; Giordano et al., 2008). Iron content has a subordinate effect wherein, relative to average peridotite (FeO_T ~8-9 wt. %), viscosity increases or decreases by ~1 log unit at lower FeO_T (0-1 wt. %) and higher FeO_T (~15 wt. %) contents, respectively (Di Genova et al., 2023). Fe redox variations generate minor variations in the viscosity of these melts that are close to measurement uncertainties (DiGenova et al., 2023; Casas et al., 2023). Lastly, scrutiny of the limited high pressure data set (7-25 GPa; Xie et al., 2021) suggests an increase in viscosity of about 0.1 log units per GPa. On this basis, our parameterization accommodates the compositional effects of H_2O and FeO_T, as well as the effects of pressure but does not consider the recently inferred effects of iron redox state.

We have fit the VFT function to the *T*(K)–log η dataset assuming that all melts converge to a common, but unconstrained, constant representing the high-T limit to melt viscosity (i.e. *A*; Russell et al., 2003; Persikov and Bukhtiyarov, 2009). The concept of a high-T limit to silicate melt viscosity is difficult to test directly because it requires observations at extreme temperatures. However, the value of *A* (constant or not) must be less than any of our physical measurements of melt viscosity (e.g., $<<10^{-1}$ Pa s for peridotitic melt). The constant *A* implies that at super-liquidus temperatures all silicate melts become highly disordered liquids, regardless of their structural arrangement at lower temperatures, and converge to a common, lower viscosity limit. At these temperatures melt viscosity becomes diffusion-driven and shows an Arrhenius-type T-dependence (e.g., Bottinga et al., 1995; Le Losq and Neuville, 2017).

In our model, therefore, each melt composition shares a common value of *A* but has unique values of *B* and *C* reflecting the effects of other variables (i.e. composition, pressure). We have expanded the terms *B* and *C* to account for two compositional variations within ultramafic melts and for pressure. The term *B* is expanded as a function of pressure:

$$B = b_0 + b_1 (P - 0.0001) \qquad (2)$$

P is the pressure in GPa. *B* is treated as independent of major element composition for the restricted range of melt compositions we consider in this model. The parameter C accounts for both variations in major element concentrations using the magnesium number (i.e. *Mg#* = MgO/[MgO + FeO_T] mol %), as well as H_2O content:

$$C = c_0 + c_1 Mg\# + c_2 X_{H2O}^{0.5} \qquad (3)$$

where X_{H2O} is the mole fraction of dissolved water. The parameter *C* is treated as independent of pressure.

The optimal solution was obtained by χ^2 minimization of the function weighted to the experimental uncertainties reported for each viscosity measurement (i.e. log $\eta_i \pm \sigma_i$):

$$\chi^2 = \sum_{i=1}^{N} \left[\left(\frac{\log \eta_i - (A + \frac{b_0 + b_1 (P_i - 0.0001)}{T_i - (c_o + c_1 Mg\#_i + c_2 X_{H2O,i})})}{\sigma_i} \right) \right]^2 \qquad (4)$$

and calibrated against 68 (i.e. *N*) viscosity measurements. The parameter A is predetermined (A = -5.4) by taking the average of values derived from fitting all of the melts individually. The optimization of Eq. 4 solves for 5 parameters for the VFT-based temperature-dependent viscosity model, including $b_{0\text{-}1}$, and $c_{0\text{-}2}$. The model values with their associated uncertainties (1σ) and the covariance matrix are listed in Table 1. The magnitudes and nature of covariances between the model parameters are summarized in the Supplementary Material.

Two other models were considered and rejected. A model where the *C* term was solely a function of Mg# (i.e. not including H_2O) was initially developed. However although it fit the experimental data well, that model predicted unreasonable (i.e. aphysical) values of melt fragility. We initially considered a model where *B* was also a function of H_2O content however, the associated model parameter had a 1σ confidence limit that included zero. Dropping that term and reducing the adjustable parameters (from 6 to 5) made no appreciable difference to the quality of the fit. A sample calculation for the viscosity for a hydrous peridotite melt at pressure is included as Supplementary Material.

4. Results

4.1 Model Parameters

The model reproduces the data well (Fig. 2A,B) and the Root Mean Square Error (RMSE) for the optimization is 0.21 log units. The average misfit for the anhydrous sample measurements is 0.17 log units and the maximum is 0.72 log units for a single sample (S34F0, Hi-Ca peridotite; DiGenova et al., 2023). The average misfit for measurements of hydrous melts (N= 7) is 0.30 log units and the maximum deviation is 0.66 log units for a single measurement (S38F5W1; DiGenova et al., 2023). The model reproduces the high-pressure data (N=5) well with an average misfit of 0.05 log units. The model VFT functions for each melt composition are well behaved and show a systematic variation with H_2O content (Fig. 2B); hydrous melts have lower viscosity and are more Arrhenian (e.g., Giordano et al., 2008), similar to the case for hydrous rhyolites (Hess and Dingwell, 1996). The model curves for high pressure ultramafic melts (Fig. 2B; green symbols) show an increase in viscosity and become more Arrhenian with pressure. The effect of increasing iron content, expressed as decreasing *Mg#*, is to cause a subordinate increase in melt viscosity.

The model high-temperature limit to melt viscosity (i.e. A) is -5.4 which is slightly lower than theoretical expected limits (i.e. -4.5 to -5; Angell, 1985) but like that found for other multicomponent silicate melts (i.e. Russell et al., 2003; Giordano et al., 2008; Li et al., 2020). The B term is related to activation energy and has a model value of 5558.3 K for anhydrous ultramafic melts at ambient pressure (*bo*; Table 1). The effect of pressure is to increase B at a rate of ~77.5 K per GPa (Fig. 2C). The base value of C for anhydrous melt, defined by c_0, is 422.9 K (Table 1) which increases weakly with increasing Mg# (i.e. c_1) and decreases strongly as a function of $X_{H2O}^{0.5}$ (Fig. 2D). The values of C converge to between 22 K and 103 K as X_{H2O} approaches 1.0 for melts having *Mg#*'s of 70 to 100, respectively (Fig. 2D).

The effects of H_2O on melt viscosity are pronounced (Fig. 3A) causing significant and continuous decreases in viscosity with increased H_2O content. As observed in other silicate melt systems (e.g., Hess and Dingwell, 1996; Schulze et al., 1996; Giordano et al., 2008), the effects of H_2O on melt viscosity are greatest at lower H_2O contents and decrease with increased H_2O content. These hydrous ultramafic melts exhibit a more Arrhenian-like temperature dependence than their anhydrous counterparts, a feature also exhibited by hydrous calcalkaline rhyolite melts (Hess and Dingwell, 1996). The viscosity of ultramafic melts increases with pressure (Fig. 3B) and the predicted increase in melt viscosity with pressure is most pronounced at lower temperatures. The corresponding curves for hydrous ultramafic melts are displaced to lower viscosity (Fig. 3B) but the relative effects of pressure on the model viscosity are the same. This results because of our assumption that B is linearly dependent on pressure and C being independent of pressure.

4.2 Transport Properties: Tg_{12} and m

Important attributes of this model for ultramafic melt viscosity are: i) it is based solely of results of high-P-T physical experimentation, ii) it accurately reproduces the original data to within experimental error, iii) it uses a minimum number of adjustable parameters (N=7), iii) it is continuous in composition (i.e. H_2O, *Mg#*), pressure, and temperature space, and iv) it independently predicts other transport properties including glass transition temperatures (Tg_{12}) and melt fragility (*m*).

We take the glass transition temperature (Tg_{12}) as the temperature (K) at which melt viscosity reaches a value of 10^{12} Pa s. Values of Tg_{12} are calculated from the parameters A, B and C predicted as a function of melt composition and pressure (Table 1):

$$Tg_{12} = \frac{B}{12 - A} + C. \qquad (5)$$

Our model independently reproduces the Tg_{12}–X_{H2O} relationship (1 atm) described by DiGenova et al. (2023) which used a Gordon-Taylor expansion constrained to match the Tg_{12} value of water, similar to the approach of Weidendorfer et al. (2023) for hydrous carbonates. Glass transition temperatures decrease nonlinearly with increased H_2O content and increase linearly with pressure (Fig. 3C). Anhydrous ultramafic melts with an Mg# of 88 have a Tg_{12} of 980 K, decrease continuously with water content, and extrapolate to a value of 390 K at $X_{H2O} = 1$. At a pressure of 25 GPa, Tg_{12} for an anhydrous melt increases to 1090 K and extrapolates with increasing water content to its limit at 501 K.

Melt fragility (m) is the measure of how rapidly viscous flow properties change with temperature as melts approach Tg_{12} (Angell, 1985). Fragility values discriminate between strong liquids (low m) having near-Arrhenian behaviour *versus* fragile melts (high m) which exhibit non-Arrhenian T-dependence (Angell, 1985). Here, we use the steepness index (m) as an estimate of melt fragility which for the VFT function can be calculated as (see Russell et al., 2022 and references therein):

$$m = \frac{B}{Tg_{12}\left(1 - {}^{C}/_{Tg_{12}}\right)^{2}}. \qquad (6)$$

The fragility of ultramafic melts decreases nonlinearly with increasing H_2O content and with increasing pressure (Fig. 3D). An anhydrous melt with an *Mg#* of 88 has a fragility of ~52 at ambient pressure *vs*. ~44 at 25 GPa. However, the rate of decrease in fragility with increasing X_{H2O} is independent of pressure.

For all systems where A is assumed to be a constant, melt fragility is limited to values > [12-A] (e.g., Russell et al., 2017; 2022) which, for this parameterization, implies a lower limit to fragility of 17.4 (Fig. 3D). Hydrous ultramafic melts at ambient pressure and at high pressure (i.e. 25 GPa) show decreasing fragility with increased water content and extrapolate to fragilities of ~31 and ~27 at X_{H2O} of 1, respectively. These extrapolated values are reasonably close to experimental estimates of fragility for low (m = 14) and high (m ~ 20–25) density water (Amann-Winkel et al. 2013). In contrast, the DiGenova et al (2023) model has a theoretical fragility limit of 14.9 (i.e. A~ -2.9) but extrapolates to negative (nonphysical) values of m at high water contents (Fig. 3D).

Pressure and H_2O content have competing and opposing effects on melt viscosity (Fig. 4A). Under isothermal conditions for a melt at 2300°C, increased H_2O content ($X_{H2O} = 0 - 0.35$) causes ~1 log unit decrease in melt viscosity at pressures of 0 – 30 GPa, whereas rising pressure causes ~1 log unit increase in viscosity. Values of Tg_{12} contoured for X_{H2O} and P show Tg_{12} to decrease by 200 – 300K for X_{H2O} of 0 to 0.35 and to increase ~100K over a pressure range of 30 GPa for a fixed H_2O content (Fig. 4B). In contrast to Tg_{12}, fragility decreases in response to increased water contents and increased pressure; values of m for anhydrous melts decrease ~40% for X_{H2O} ~0.35 at all pressures (Fig. 3D, 4C).

The relationships between Tg_{12} and m as a function of pressure and H_2O content are summarized in Figure 5 for an ultramafic melt with an Mg# of 88. At constant pressure (Fig. 5, dashed lines for 5 to 30 GPa), Tg_{12} and m decrease with increased H_2O content, whereas at constant water content (Fig. 5, blue lines), Tg_{12} increases with pressure whilst m decreases with pressure. We have also compared our predictions for anhydrous peridotite to model values of Tg_{12} and m for anhydrous diopside (NBO/T = 2) as a function of pressure (Fig. 5, heavy black line). Li et al. (2020) developed a pressure dependent model for predicting the viscosity of anhydrous melts in the system Albite-Anorthite-Diopside. Their model predicts a pressure-dependent trend in Tg_{12}–m values for diopside melt that parallels the values we independently predict for anhydrous ultramafic melts (Fig. 5). Both models predict an increase in Tg_{12} with pressure and a concomitant decrease in fragility whereas for more polymerized melts, albite and anorthite (i.e. NBO/T =0), Li et al. (2020) predicted an increase in melt fragility with pressure.

4.3 Filling a Gap in Knowledge

Our model is a means of predicting the viscosity of ultramafic melts over a wide range of geological conditions (T, P, $Mg\#$, X_{H2O}). These melt compositions are pertinent to many magmatic, volcanic, and tectonic processes. As discussed by DiGenova et al. (2023) previously published models for silicate melt viscosity fail to reproduce measurements on ultramafic melts (see Supplement Material for full discussion). In that regard, our model fills a gap in knowledge and is a means to explore the properties and behaviour of these melts within a variety of terrestrial and extra-terrestrial environments. We use $Mg\#$ as a proxy for compositional variations in ultramafic melts and this supports the model's use for melts having MgO contents in excess of 20 wt. % and over a range of Mg:Fe ratios (i.e. Mg# 70-100). This includes melt compositions spanning pyrolite, peridotite and komatiites.

Two models that account for the effects of pressure on melt viscosity (Persikov and Bukhtiyarov, 2009; Duan, 2014) fail to predict the viscosity of ultramafic melts at ambient or high-pressure (see Supplementary Material). Our calibration for pressure relies on the most recent, but limited (N=5), dataset of Xie et al. (2021) who used in-situ falling sphere viscometry to measure peridotite melt viscosity at 7 to 25 GPa. Our model accurately reproduces both the high- and low-pressure datasets as well as reproducing the pressure dependence that is implicit in the high-P data to within error. This can be illustrated by fitting the Xie et al. (2021) dataset to an Arrhenian model:

$$\log \eta = A_x + \frac{Bo_x + Bp_x \times P}{T(K)} \qquad (7)$$

where A_x (-6.36), Bo_x (10053.8), and Bp_x (105.5) are adjustable parameters and Bp_x provides a linear dependence on pressure (P in GPa). As would be expected, the simple Arrhenian model (Eq. 7) reproduces the original data well (Fig. 6A; dashed lines). The isothermal viscosity curves predicted as a function of P, at the temperature of each experiment, intersect each datapoint (i.e. log η : P). Our model also assumes a linear pressure dependence for *B* (see Table 1; $b_2 = 84.2$) and isothermal curves from our model (Fig. 6A; solid lines) reproduce the Xie et al. (2021) data equally well. Furthermore our model extrapolates slightly better to the 1 atm data of Dingwell et al. (2004).

We elected not to calibrate our model using the high-pressure measurements of ultramafic melt viscosity reported by Liebske et al. (2005) and Brown (2012). We made this decision because of the significantly larger scatter in their data (as previously observed by Xie et al., 2021; Huang et al., 2024) when compared to the more precise ambient-pressure measurements ($\pm 0.08 - 0.25 \log_{10} \eta$) and the more coherent character of the data from Xie et al. (2021). Their data, however, do provide an independent test of our model.

Liebske et al. (2005) used in-situ falling sphere experiments to provide measurements of viscosity for peridotite melts at temperatures of 1750 – 2250 ^{o}C and pressures of 2 – 13 GPa (Fig. 6). The experiments are identified as being in Cell A and B or in Cell C. The latter set-up (Cell C) featured a slightly different geometry (i.e. shorter travel distance) which resulted in fewer snapshots of the falling spheres (pers comm.; C. Liebske, April 2024; Xie et al., 2021) and, thus, less precision (see Kono, 2018; Ashley et al., 2024) and more potential scatter (Fig. 6B). Our model predicts most of their data to within 0.25 log units and all data to within 0.5 log units.

The high-pressure viscosity data of Brown (2012) are for two different komatiite melts at temperatures of ~1570 – 2200K and pressures of 1 – 10.8 GPa. Our model reproduces most of the viscosity data for the Barberton komatiite to within 0.25 log units but fails to reproduce the Gorgona komatiite data (Fig. 6B). This discrepancy between model and data is because the Gorgona komatiite lies outside the compositional range of our calibration. Although it has an Mg# of 74 (within out model range), the MgO content is too low (< 18 wt. %) and outside of our model range (25 < MgO wt. % < 41).

5. Discussion

5.1 Pressure dependence of viscosity for depolymerized melts (NBO/T >2)

A benefit of predictive models calibrated on observations or direct physical measurements is that they can be interrogated for additional insights. This model, for example, allows for the calculation and independent prediction of ancillary properties of silicate melts, such as glass transition temperatures and melt fragility. These values can be compared against values measured directly by calorimetric or spectroscopic methods, respectively (e.g., Di Genova et al., 2023). Robust models calibrated on high quality data and fit to a minimum number of adjustable parameters commonly allow for reliable extrapolation beyond the original data. This provides insights into parameter spaces that have yet to be explored experimentally.

The effect of pressure on melt viscosity is important for constraining the properties of mantle and crustal melts and for modelling their origins, transport, and the processes that govern their thermochemical evolution. An in-depth discussion of the effects of pressure on silicate melt viscosity, including structural effects on melt viscosity, is afforded by the review papers of Sakamaki and Ohtani (2022) and Kono (2018). Our model is consistent with the viscosity of ultramafic silicate melts being linearly dependent on pressure (Fig. 6C-D); the model reproduces the (limited) available high-pressure data and extrapolates to reasonable values beyond the original database. Several MD simulations have suggested, however, that fragile, depolymerised silicate melts, including basalt (i.e. Bajgain et al., 2022) and peridotite (i.e. Huang et al., 2024), show non-linear variations in melt viscosity with increasing pressure. At present the experimental data do not support a higher order treatment for pressure which is best tested by additional physical experimentation. Furthermore, we have no idea if extrapolation of the model's pressure effect at undercooled conditions is sound; for example, we have no data that inform on the effect(s) of pressure at temperatures close to *Tg*. The pressure dependence of viscosity for fragile melts could be very different near *Tg* due to temperature-driven changes in melt structure.

The experimental results and model proposed by Liebske et al. (2005) bear additional comment because of its implications for the pressure dependence of melt viscosity. Their analysis of the experimental data led them to suggest that there was a maximum in viscosity at ~7–8 GPa followed by a steady decrease with pressure (see Fig. 3 in Liebske et al., 2005). On that basis they proposed a VFT-based model which expressed *B* as a 3rd order polynomial in *P*. Their model results in a maximum viscosity at 7–10 GPa and then a monotonic decrease to unrealistic values which precludes extrapolation beyond their original data (grey lines; Fig. 6C-D). However, we see no suggestion of a maximum in melt viscosity in the experimental datasets nor in our model (black lines; Fig. 6C-D). The maximum in viscosity and the negative P-dependence proposed by Liebske et al. (2005) is mainly driven by data derived from Cell C which show more scatter (Fig. 6B) and may be less precise (see Ashley et al., 2024). Clearly, additional experiments designed to inform on this issue are needed in lieu of further speculation or discussion at this time.

There is general consensus on the behaviour of viscosity with increasing pressure for polymerised melts (NBO/T < 1) where a negative pressure dependence can occur between 1 and 13 GPa before increasing with additional pressure (Wang et al., 2014; Sakamaki and Ohtani, 2022). For depolymerised melts with an NBO/T > 2, viscosity is weakly dependent on P and generally increases (monotonously) with pressure at isothermal temperatures (see Wang et al., 2014; Sakamaki and Ohtani, 2022; Xie et al., 2021). Recent experimental work on simple depolymerised melts, including: i) Spice et al. (2015) on Fe_2SiO_4 melts (NBO/T = 4) and ii) Cochain et al. (2017) on $MgSiO_3$ (NBO/T 1.75-1.96) and $CaSiO_3$ (NBO/T = 1.92-2.12) melts, have suggested a weak negative pressure dependence up to 13 GPa. In contrast, the molecular dynamic simulation studies of melt viscosity by Zhang et al. (2010; $MgSiO_3$ and $CaSiO_3$ melts) and Sun et al. (2018; Fe_2SiO_4), and simulations of Mg_2SiO_4 melt viscosity by Adjaoud et al. (2008) and Drewitt et al. (2022) argue for a continuous increase in viscosity with increasing P. The most recent MD simulation data by Dufils et al. (2018) and Huang et al. (2024) on multicomponent ultramafic melts (NBO/T > 2), including komatiite, peridotite, and pyrolite, also show a continuous increase in viscosity with pressure. These latter results are fully consistent with our experimentally constrained predictive model.

5.2 Mantle melts and viscosity

A unique strength of this model is to predict the viscosity of mantle melts at mantle temperature-pressure conditions. The viscosity values calculated for an anhydrous and hydrous (5 mol% H_2O) ultramafic peridotitic melt (Mg# ~88) are plotted as a function of the temperature-pressure conditions defined by the liquidus for a fertile mantle composition (KLB-1; Fig. 7). Melt viscosity at the surface is ~1 – 1.5 Pa s and shows a slight decrease (~0.5 log units) with increasing T and P to the base of the lithosphere after which viscosity remains nearly constant (Fig. 7B). Whilst the effect of pressure is to increase viscosity, the corresponding rise in temperature with depth compensates. The pattern is the same for anhydrous and hydrous melts; a 5 mol% H_2O content simply reduces melt viscosity by ~0.5 log units. For comparison, we calculated the melt viscosity at the same mantle liquidus temperatures but without accounting for the effects of pressure (i.e. b_1 set to 0; Table 1). Ignoring the effect of pressure on the viscosity of ultramafic melts would erroneously suggest a near linear continuous decrease in viscosity (Fig. 7B; ~2 orders of magnitude over 30 GPa).

The Arrhenian model of Shaw (1972) has commonly been used to calculate the viscosity of the magma ocean. Shaw's model is quite robust for silicate melts (anhydrous and hydrous) at high temperatures where melts show Arrhenian behaviour (Russell et al., 2022) although, here, it predicts viscosity values at surface temperatures ~1.5 log units higher than the present model. The Shaw (1972) model does not account for pressure and, therefore, also predicts a linear decrease in viscosity as a function of mantle temperature that is too high at upper mantle conditions and too low below the transition zone. More importantly it predicts a negative gradient in viscosity that could significantly impact calculated values of melt mobility (i.e. ratios of η/ρ) at high mantle pressures.

We have extrapolated our model well beyond the calibration dataset (see caption Fig. 7C) to predict melt viscosity at depths and pressures (0–150 GPa) found in the early Earth's magma oceans (Fig. 7C). We have adopted the P-T array of Huang et al. (2023; modified from Fiquet et al., 2010) to represent the temperature distribution with depth in the magma ocean. The change in temperature with depth is normalized and plotted as [1−T/T_{150GPa}] where T_{150GPA} is the maximum temperature located at 150 GPa (dashed line; Fig. 7C).

Our model has constant values of *A* and *C* (for a fixed H_2O content), and the *B* parameter rises from 5558 K to 17,957 K over 160 GPa. The model values of viscosity for anhydrous and hydrous (5 mol%) peridotitic melts are calculated along the P-T array and show a pronounced (0.5-1 log units) decrease to a pressure of ~40 GPa before increasing steadily at a lower rate. The complex pattern in melt viscosity reflects the interplay between temperature and pressure effects on viscosity dictated by the shape of the adopted P-T array in the magma ocean. The steep rise in temperature in the shallow mantle drives the melt to a low extreme but once the temperature gradient shallows the effect of pressure begins to dominate driving the melt viscosity back to higher values.

For comparison we show two model viscosity curves derived from MD simulations and using the same P-T array. Huang et al. (2024) fit VFT-based polynomial equations to a series of MD simulations of peridotitic melt viscosity at temperatures of 2200, 3000, 4000 and 6000K over the pressure range of 1–159 GPa. They proposed two separate equations for the P-T dependence of viscosity for the temperature intervals 2200 – 3000 K and 4000 – 6000K, which are connected by a dashed line in Figure 7C. The two model expressions have constant values of *C* but pressure dependent expressions for *A* and *B*. In the lower temperature equation, values *A* and *B* vary with pressure up to 160 GPa as -5.93 to -27.3, and 748 to 62,916, respectively. The higher temperature expression implies ranges of *A* and *B* of -7.1 to -10.3, and 1414 to 28,726, respectively.

We used the dataset derived from MD simulations of peridotite (PHN1611) melt viscosity reported by Dulfis et al. (2018) to create a pressure dependent VFT-based model (i.e., log n = -

2.39 + [523.7 + 22.04 P(GPa)]/[T(K) - 1557]). This simple model reproduces the MD dataset and has an RMSE of 0.025 and an average and maximum misfit of 0.019 and 0.05 log units, respectively. The model for the MD simulations of Dulfis et al. (2018) has constant A and C parameters, whilst B rises from 524 to 4030 over 160 GPa. Our VFT-fit to their data is used to plot another MD-based viscosity curve for the early Earth magma ocean as a function of the peridotite P-T liquidus (Fig. 7C).

The model curves for the two MD datasets (i.e. Huang et al., 2024; Dulfis et al., 2018) show a similar decrease in viscosity within the upper mantle due to the steep temperature gradient. The model curves define viscosity minima in the early Earth molten mantle at 11 and 34 GPa, respectively (*versus* ~40 GPa for our model). At pressures greater than 1 GPa, the two MD models predict a total range in (anhydrous) melt viscosity of ~0.3-0.4 log units whereas our model for anhydrous and hydrous peridotitic melts predicts a total range in viscosity of 0.8 log units. The Huang et al. model agrees reasonably well with ours in two areas: i) ~ 25 GPa where we have data (heavy line segments), and ii) at depth (high-T and P) where the MD simulations are optimal, and our model is extrapolated well past the calibration data. The largest deviation is found at ~40-50 GPa which coincides with temperatures between Huang's two predictive equations and pressures just outside of our calibration (Fig. 7C). The Dulfis et al. (2018) MD-based model is nearly parallel to the Huang et al. model but predicts viscosities ~0.25-0.5 log units higher along the early Earth peridotite liquidus curve.

6. Conclusions

Beyond the Earth and terrestrial planets lies the rapidly growing realm of discovery of exoplanets. These objects number in their thousands already with no end in sight of their growing number. One of the major data sets being accumulated on these planetary bodies is that of the chemistry, including identification of gas species, in their planetary exospheres (e.g., Heng and Showman, 2015). Models that are being developed for atmospheric chemistry of exoplanets must in future rely on a more robust set of models for the processes of planetary degassing and these processes in turn will rely for many exoplanets on the understanding of the behavior of ultramafic melts at depth or at the surface of the exoplanet (both at variable pressures). With the model presented here we hope to have contributed to a path towards the modelling of ultramafic planetary liquids and their degassing behavior.

CrediT authorship contribution statement

J.K. Russell: Conceptualization, modelling, data analysis, writing. **K-U Hess**: Data compilation, literature review, model evaluation and comparison, writing. **D.B. Dingwell:** Data assessment, implications, writing, reviewing.

Declaration of competing interest

The authors declare they have no competing financial interests or personal relationships that could have appeared to influence the work reported herein.

Acknowledgments

This study was supported by the Natural Sciences and Engineering Research Council of Canada (NSERC) Discovery Grants program (JKR: 2018-03841) and by the Alexander von Humboldt Foundation through a Carl Friedrich von Siemens Research Award. DBD acknowledges the support of 2018 ERC Advanced Grant 834255 (EAVESDROP). We are indebted to C. Liebske, C. LeLosq, and P. Asimow for critical reviews of our manuscript which has helped us clarify and strengthen our arguments.

Appendix A. Supplementary material

Supplementary material related to this article can be found on-line at x-xxxxx.

References Cited

Adjoud, O., Steinle-Neumann, G., Jahn, S., 2008. Mg_2SiO_4 liquid under high pressure from molecular dynamics. Chem. Geol. 256, 185-192.

Al-Mukadam, R., Di Genova, D., Bornhoft, H., Deubener, J., 2020. High-rate calorimetry derived viscosity of oxide melts prone to crystallization. J. Non-Crystalline Solids 536, 119992, https://doi.org/10.1016/j.jnoncrysol.2020.119992.

Amann-Winkel, K., Gainaru, C., Handle, P.H., Seidl, M., Nelson, H., Böhmer, R., Loerting, T., 2013. Water's second glass transition. Proc. Nat. Acad. Sci. 110, 17720-5. doi: 10.1073/pnas.1311718110.

Angell, C.A., 1985. Strong and fragile liquids. In K. L. Ngai and G. B. Wright, Eds., Relaxations in Complex Systems. pp. 3–11, U.S. Department of Commerce National Technical Information Service.

Arndt, N., 2003. Komatiites, kimberlites and boninites. J. Geophys. Res. 108, B6 2293. 10.1029/2002JB002157. hal-00097430.

Ashley, A. W., Mookherjee, M., Xu, M., Yu, T., Manthilake, G., Wang, Y., 2024. Viscosity measurements at high pressures: A critical appraisal of corrections to Stokes' Law. J. Geophys. Res. 129, e2023JB028489. https://doi.org/10.1029/ 2023JB028489

Bajgain, S.K., Ashley, A.W., Mookherjee, M. 2022. Insights into magma ocean dynamics from the transport properties of basaltic melt. Nature Communications 13, 7590 (2022). https://doi.org/10.1038/s41467-022-35171-y.

Brown, L.OD. 2012. Viscosities of Silicate Liquids at High Pressures. Unpublished PhD Thesis, University of California, Davis.

Casas, A.S., Hess, K-U., Badro, J., Eitel, M., Dingwell, D.B., 2023. A redox effect on the viscosity of molten pyrolite. Chem. Geol. 642, 121816 https://doi.org/10.1016/j.chemgeo.2023.121816.

Cochain B., Sanloup C., Leroy C., Kono Y., 2017. Viscosity of mafic magmas at high pressures. Geophys. Res. Lett. 44, 818-826.

deVries, J., Nimmo, F., Melosh, H.J., Jacobson, S.B., Morbidelli, A., Rubie, D.C., 2016. Impact-induced melting during accretion of the Earth. Progress in Earth and Planetary Science, 3, 7.

Drewitt, J.W.E. Walter, M.J. Brodholt, J.P. Muir, J.M.R., Lord, O.T., 2022. Hydrous silicate melts and the deep mantle H2O cycle. Earth Planet. Sci. Lett. 581, 117408, ISSN 0012-821X, https://doi.org/10.1016/j.epsl.2022.117408.

DiGenova, D., Bondar, D., Zandonà, A., Valdivia, P., Al-Mukadam, R., Fei, H., Withers, A.C., Ballaran, T.B., Kurnosov, A., McCammon, C., Deubener, J., Katsura, T., 2023. Viscosity of anhydrous and hydrous peridotite melts. Chem. Geol. 625, 121440, doi.org/10.1016/j.chemgeo.2023.121440.

Dingwell, D.B., Courtial, P., Giordano, D., Nichols, A.R.L., 2004. Viscosity of peridotite liquid. Earth Planet. Sci. Lett. 226, 127–138. https://doi.org/10.1016/j. epsl.2004.07.017.

Duan, X., 2014. A model for calculating the viscosity of natural iron-bearing silicate melts over a wide range of temperatures, pressures, oxygen fugacities, and compositions. Am. Mineral. 99, 2378–2388.

Dufils, T. Sator, N. Guillot, B., 2018. Properties of planetary silicate melts by molecular dynamics simulation. Chem. Geol. 493, 298-315.

Fiquet, G., Auzende, A. L., Siebert, J., Corgne, A., Bureau, H., Ozawa, H., Garbarino, G., 2010. Melting of peridotite to 140 gigapascals. Science 329, 1516–1518. https://doi.org/10.1126/science.1192448

Fulcher, G.S., 1925. Analysis of Recent Measurements of the Viscosity of Glasses. Journal of the Am. Ceramic Soc. 8, 339-355. https://doi.org/10.1111/j.1151-2916.1925.tb16731.x

Giordano, D., Dingwell, D.B., 2003. Viscosity of hydrous Etna basalt: implications for Plinian-style basaltic eruptions. Bull. Volcanol. 65, 8–14.

Giordano, D., Russell, J.K., Dingwell, D.B., 2008. Viscosity of magmatic liquids: a model. Earth Planet. Sci. Lett. 271, 123–134, https://doi.org/10.1016/j.epsl.2008.03.038.

Gottsmann, J., Giordano, D., Dingwell, D.B., 2002. Predicting shear viscosity during volcanic processes at the glass transition: A calorimetric calibration. Earth Planet. Sci. Lett. 198, 417 - 427.

Grove, T.L., Parman, S.W., 2004. Thermal evolution of the Earth as recorded by komatiites. Earth Planet. Sci. Lett. 219, 173-187.

Hess K-U, Dingwell DB, 1996. Viscosities of hydrous leucogranitic melts: A non-Arrhenian model. Am. Mineral. 81, 1297-1300.

Heng, K., Showman, A.P., 2015. Atmospheric Dynamics of Hot Exoplanets. Ann. Rev. Earth Planet. Sci. 43:1, 509-540.

Huang, D., Li, Y., & Murakami, M. (2024). Low viscosity of peridotite liquid: Implications for magma ocean dynamics. Geophys. Res. Lett. 51, e2023GL107608. https://doi.org/10.1029/2023GL107608

Hui, H., Zhang, Y., 2007. Toward a general viscosity equation for natural anhydrous and hydrous silicate melts. Geochim. Cosmochim. Acta 71, 403–416.

Jones, T.J., Russell, J.K., Brown, R.J., Hollendonner, L., 2022. Melt stripping and agglutination of pyroclasts during the explosive eruption of low viscosity magmas. Nature Comm. 13, 992, https://doi.org/10.1038/s41467-022-28633-w.

Kono, Y., 2018. Chapter 10: Viscosity Measurement, *in* Magmas Under Pressure (Kono, Y. and Sanloup, C.) Elsevier, p. 261-280, ISBN 9780128113011, https://doi.org/10.1016/B978-0-12-811301-1.18001-3.

Li, M., Russell, J.K., Giordano, D., 2020. Temperature-pressure-composition model for melt viscosity in the Dp-An-Ab system. Chem. Geol. 560, doi.org/10.1016/j.chemgeo.2020.119895

Liebske, C., Schmickler, B., Terasaki, H., Poe, B.T., Suzuki, A., Funakoshi, K-I., Ando, R., Rubie, D.C., 2005. Viscosity of peridotite liquid up to 13 GPa: Implications for magma ocean viscosities. Earth Planet. Sci. Lett. 240, 589-604.

Moss, S., Russell, J.K., 2011. Fragmentation in kimberlite: products and intensity of explosive eruption. Bull. Volc. 73, 983–1003, https://doi.org/10.1007/s00445-011-0504-x

Mysen, B.O., Virgo, D., Seifert, F.A. 1982. The structure of silicate melts: implications for chemical and physical properties of natural magma. Rev. Geophys. 20, 353–383.

Mysen, B.O., 1988. Structure and Properties of Silicate Melts. Amsterdam, Elsevier.

Persikov, E.S., Bukhtiyarov, P.G., 2009. Interrelated structural chemical model to predict and calculate viscosity of magmatic melts and water diffusion in a wide range of compositions and T-P parameters of the Earth's crust and upper mantle. Russian Geology and Geophysics, 50, 1079-1090.

Putirka, K.D., Xu, S., 2021. Polluted white dwarfs reveal exotic mantle rock types on exoplanets in our solar neighborhood. Nature Comm. 12:6168. doi: 10.1038/s41467-021-26403-8. PMID: 34728614; PMCID: PMC8563750.

Richet, P., 1984. Viscosity and configurational entropy of silicate melts. Geochimica Cosmochimica Acta, 48, 471-483.

Russell, J.K., Giordano, D., 2017. Modelling configurational entropy of silicate melts. Chem. Geol. 461, 140-151, https://doi.org/10.1016/j.chemgeo.2016.07.019.

Russell, J.K., Giordano, D., Dingwell, D.B., 2003. High-temperature limits on viscosity of non-Arrhenian silicate melts. Am. Mineral. 88, 1390-1394.

Russell, J.K., Hess, K-U, Dingwell, D.B., 2022. Models for viscosity of geological melts. Rev. Mineral. Geochem. 87: 841–885. doi: https://doi.org/10.2138/rmg.2022.87.18

Sakamaki, T. Ohtani, E., 2022. High Pressure Melts. Rev. Mineral. Geochem. 87: 557–574. doi: https://doi.org/10.2138/rmg.2022.87.11

Scherer, G.W., 1984. Use of the Adam-Gibbs equation in the analysis of structural relaxation. J. Am. Ceram. Soc. 67, 504–511.

Schulze, F., Behrens, H., Holtz, F., Roux, J., Johannes, W., 1996. The influence of H_2O on the viscosity of a haplogranitic melt. Am. Mineral. 81, 1155-1165, https://doi.org/10.2138/am-1996-9-1014.

Shaw, H.R., 1972. Viscosities of magmatic silicate liquids; an empirical method of prediction. Am. J. Sci. 272, 870–893.

Spice H., Sanloup C., Cochain B., de Grouchy C., Kono Y., 2015. Viscosity of liquid fayalite up to 9 GPa. Geochim. Cosmochim. Acta 148, 219-227.

Sun, Y., Zhou, H., Yin, K., Zhao, M., Xu, S., Lu, X., 2018. Transport properties of Fe_2SiO_4melt at high pressure from classical molecular dynamics: Implications for the lifetime of the magma ocean. J. Geophys. Res. 123, 3667–3679. https://doi.org/10.1029/2018JB015452

Wang, Y., Sakamaki, T., Skinner, L., et al., 2014. Atomistic insight into viscosity and density of silicate melts under pressure. Nature Comm. DOI: 10.1038/ncomms4241, 1-10.

Weidendorf, D., Hess, K-U., Ruhekenya, R., Schawe, J., Wilding, M., Dingwell, D., 2023. Effect of water on the glass transition of a potassium-magnesium carbonate melt. Phil. Trans. Roy. Soc. A 381, http://doi.org/10.1098/rsta.2022.0355.

Xie, L., Yoneda, A., Katsura, T., Andrault, D., Tange, Y., Higo, Y., 2021. Direct viscosity measurement of peridotite melt to lower-mantle conditions: A further support for a fractional magma-ocean solidification at the top of the lower mantle. Geophys. Res. Lett. 48, e2021GL094507. https://doi. org/10.1029/2021GL094507.

Zhang, L. Van Orman, J.A. Lacks, Daniel J., 2010. Molecular dynamics investigation of MgO–CaO–SiO2 liquids: Influence of pressure and composition on density and transport properties. Chem. Geol. 275, 50-57.

Figure Captions

Figure 1. Compiled experimental database of ultramafic melts used to calibrate predictive model. (A) Data plotted as log η (Pa s) *vs*. 10000/T(K) where symbols denote measurements of anhydrous (grey), hydrous (blue) and anhydrous high-pressure (green) melts. Data of Liebske et al. (2005; crosses) were not used in the calibration. Compositional range of compiled ultramafic melts expressed as (B) Al_2O_3 *vs*. SiO_2/(MgO+FeO); (C) Mg# *vs*. H_2O content; and (D) SM *vs*. NBO/T indices.

Figure 2. Results of model optimization. (A) Comparison of predicted values of log η (Pa s) to measured values. Dashed lines denote ± 0.5 log units. (B) Model VFT curves (solid lines) calculated (see Table 1) for each melt composition and compared to data (see Supplementary Materials). VFT curves for high-pressure data are calculated at their experimental pressures (i.e. Xie et al., 2021). (C) Model values of *B* as a function of pressure (1 atm to 25 GPa). Note *B* is independent of H_2O content and Mg#. (D) Model values of *C* as a function of X_{H2O} for ultramafic melts having Mg#'s from 70 to 100. Solid line is for a melt with Mg# of 88. Note *C* is independent of pressure.

Figure 3. Model predictions for an ultramafic melt (Mg# = 88). (A) Temperature-dependent curves of melt viscosity for H_2O contents of 0 (anhydrous) to 30 mol%. (B) The effect of pressure on model VFT curves for an anhydrous and hydrous (5 mol%) ultramafic melt. (C) Values of Tg_{12} (K) (i.e. $\eta = 10^{12}$ Pa s) predicted as a function of X_{H2O} (solid black line) at 1 atm; dashed black lines show increase in Tg_{12} with increased pressure. Model 1 atm. values from DiGenova et al. (2023) are shown by red dashed line. Values for anhydrous and hydrous melts in compiled dataset are shown as grey and blue coloured symbols, respectively. (D) Values of fragility predicted as a function of X_{H2O} (solid black line); dashed black lines show decrease in melt fragility with increasing pressure. Red dashed line is 1 atm. model of DiGenova et al. (2023). Grey shaded line denotes the lower limit in melt fragility predicated by a constant value of *A* (i.e. -5.4; Russell et al., 2017; 2022).

Figure 4. Contour maps of effects of pressure (*P*) and H_2O content (X_{H2O}) on transport properties of a fixed ultramafic melt composition (Mg# = 88). (A) Contours of isothermal (2300 °C) melt viscosity decrease with H_2O content and increase with P. (B) Contour plot showing increase in Tg_{12} values with increasing *P* and a decrease with increasing X_{H2O}. (C) Fragility (*m)* contours show decrease from ~50 to ~32 with increasing X_{H2O} and *P*.

Figure 5. Graphical summary of variations in Tg_{12} (K) and melt fragility (*m*) as a function of H_2O content (0-30 mol%) and *P* (0-25 GPa). Predicted Tg_{12} (K) increases with rising *P* and decreases strongly with increased H_2O. Melt fragility (*m*) decreases with increased H_2O content and increased *P*. Solid black line is for anhydrous diopside melt as predicted by model of Li et al. (2021) and shows a similar rise in Tg_{12} (K) and decrease in melt fragility (*m*) with increased P (0-25 GPa).

Figure 6. *P*-dependence of predicted and observed viscosity of peridotite melts. (A) Isothermal values of viscosity predicted by this model (Table 1; solid lines) and values predicted by an Arrhenian model (dashed lines) fitted to the original high *P* measurements of Xie et al. (2021;

black symbols; see text). (B) Comparison of high *P* data sets not used to calibrate the model *versus* the values predicted by our model; data of Xie et al. (2021) were used to calibrate the effects of pressure and are shown here for comparison. Non-calibration high *P* datasets include experiments of Liebske et al. (2005) and Brown (2012). Dashed lines indicate ± 0.25 log units. (C) Isothermal values (2000K and 2800K) of viscosity predicted for a range of P (0 - 30GPa). Model lines are for this work (solid black; blue lines for 5 mol% H_2O), model of Liebske et al. (2005; grey lines), and Dingwell et al. (2004; 1 atm model). Shaded fields indicate the range of data used to calibrate the two models: i) Liebske et al. (2005; yellow, solid outline) and ii) this model (green, dashed outline). (D) Model values of Tg_{12} (K) for a range of P (0 - 30GPa) as discussed in (C).

Figure 7. Predicted viscosity of ultramafic melts at mantle conditions. (A) Mantle *T* distributions to 30 GPa in modern Earth for fertile mantle composition (KLB-1; modified from Grove and Parman, 2004) at solidus (S) and liquidus (L) conditions. Thin lines show rise in predicted Tg_{12} (K) values with *P* for anhydrous (black) and hydrous (5 mol%, blue) melt. (B) Heavy lines denote melt viscosity calculated at KLB-1 liquidus *T* and *P* (Panel A). Dashed lines are melt viscosities where the effects of P are not accounted for. Thin solid lines are anhydrous and hydrous viscosity values predicted by Shaw (1972). (C) Melt viscosity for an early Earth magma ocean at liquidus conditions and deep mantle pressures (P-T array from Fiquet et al., 2010; Huang et al., 2023). (1) Viscosity calculated with this model for anhydrous and hydrous peridotitic melt. (2) Viscosity of peridotitic melt predicted by Huang et al. (2023); dashed line is extrapolation between 2 functions for different temperature regimes. (3) Model curve for peridotite melt viscosity-based MD simulations reported by Dulfis et al. (2018; see text). Heavy line segments (1, 2, and 3) indicate range of pressures over which models were calibrated. Dashed black line denotes mantle temperature scaled as $\Delta T = 1 - T/T_{150GPa}$.

Table 1. Model parameters for VFT-based temperature-dependent viscosity of anhydrous and hydrous ultramafic melts[1].

$$\log \eta = A + [b_0 + b_1 (P-0.0001)] / [T - (c_0 + c_1\, Mg\# + c_2\, X_{H2O}^{0.5})]$$

Parameters	**Values**	**± σ**
A	-5.4	0.2
b_0	5558.3	106
b_1	77.49	12
c_0	422.93	9.2
c_1	2.69	0.1
c_2	-589.4	13

Covariance Matrix

	b_0	b_1	c_0	c_1	c_2
b_0	11163				
b_1	-495	147			
c_0	-663	30	84		
c_1	-0.30	0.01	-0.49	0.01	
c_2	-634	29	42	-0.06	175

---

[1] Model optimization has MSE of 0.045 and RMSE of 0.21

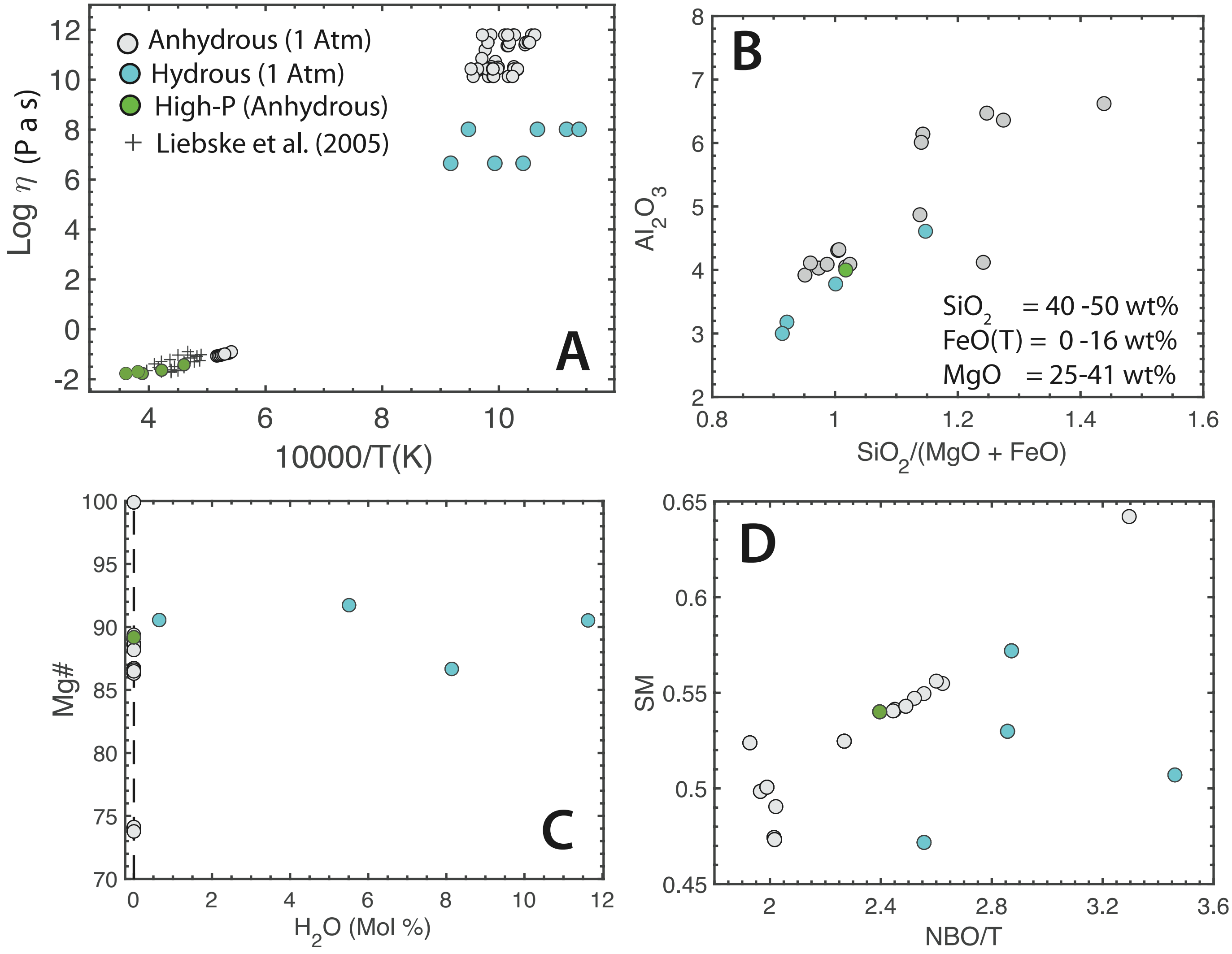

Figure 1. Ultramafic melt viscosity, 2024)

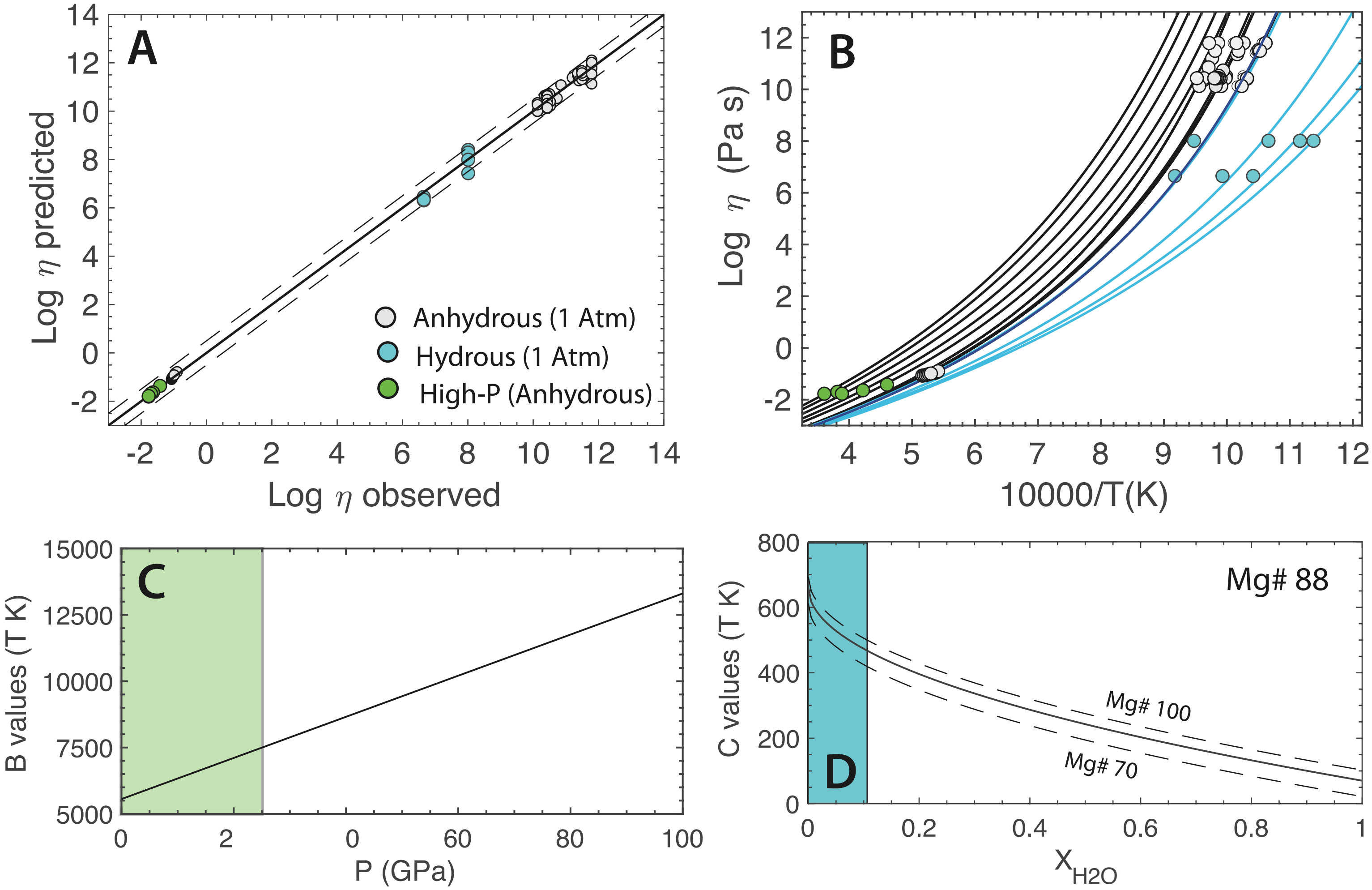

Figure 2. Ultramafic melt viscosity, 2024

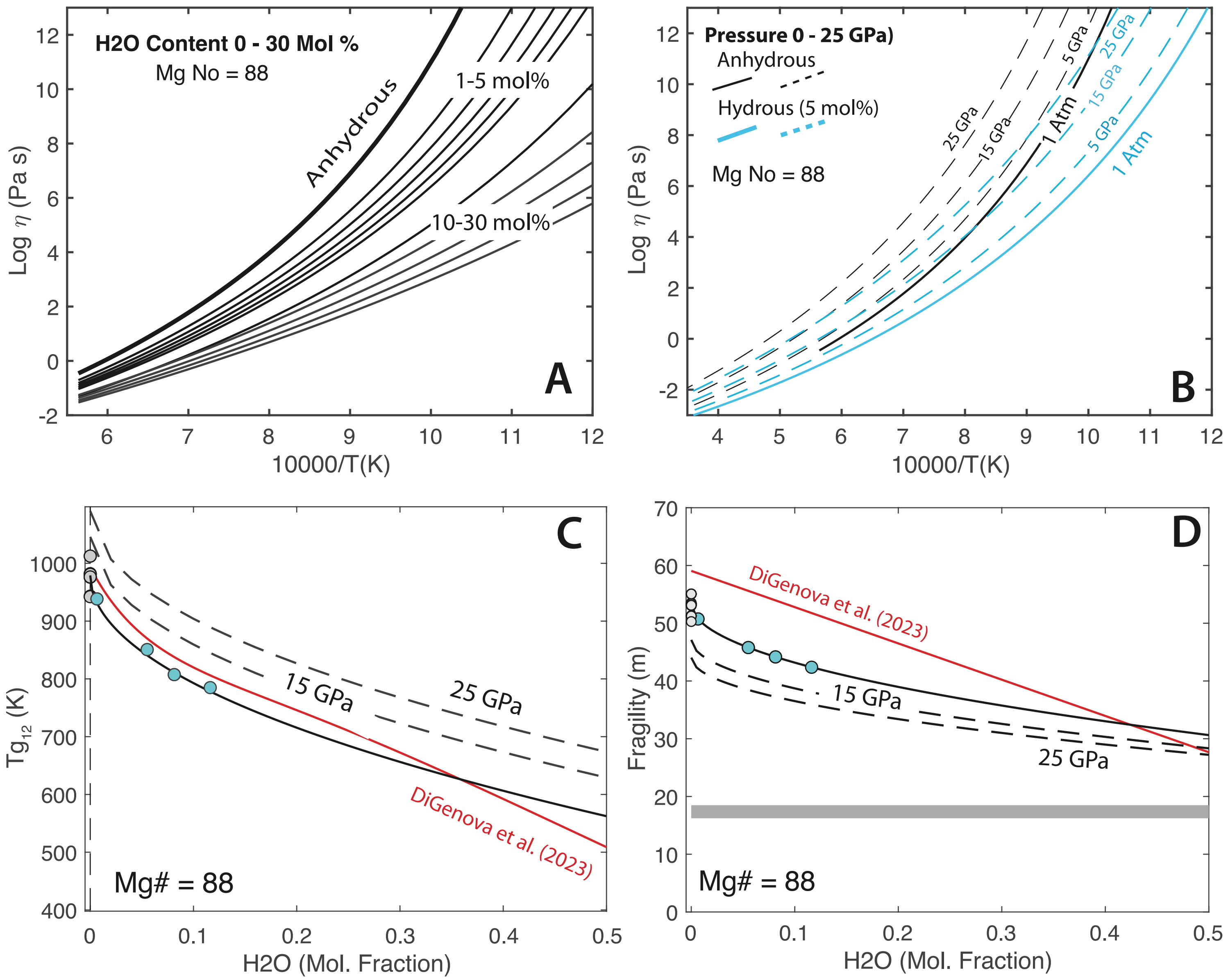

Figure 3. Ultramafic melt viscosity, (2024)

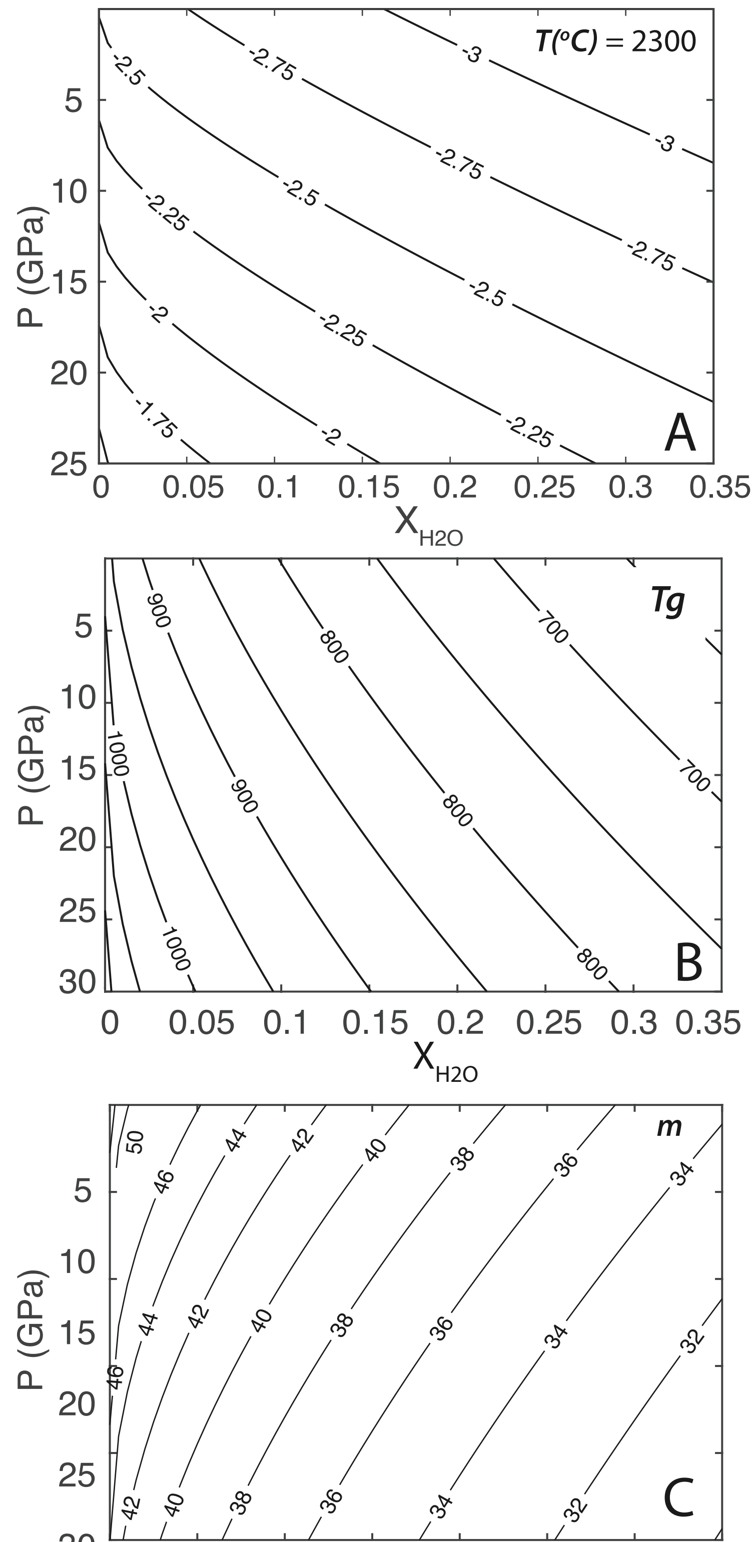

Figure 4. Ultramafic melt viscosity, 2024

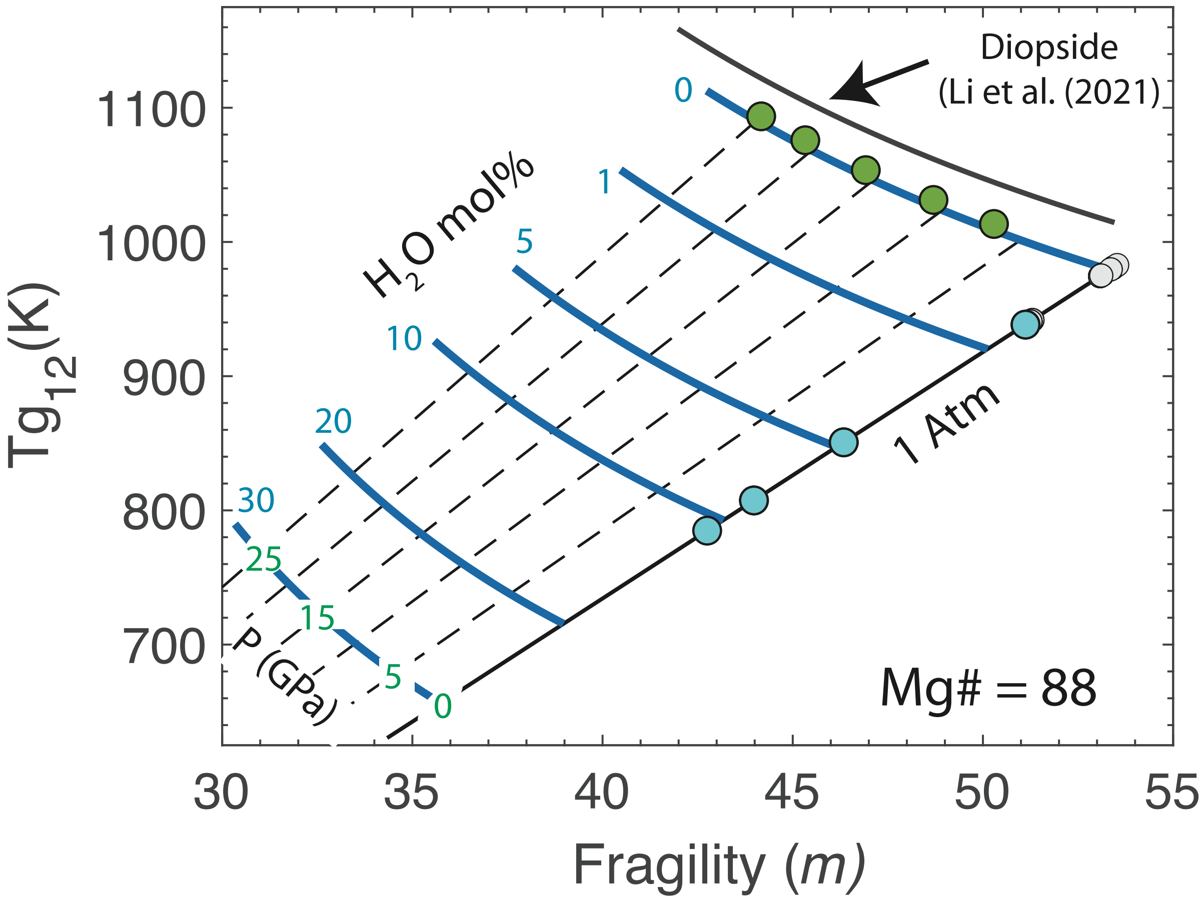

Figure 5. Ultamafic melt viscosity, 2024

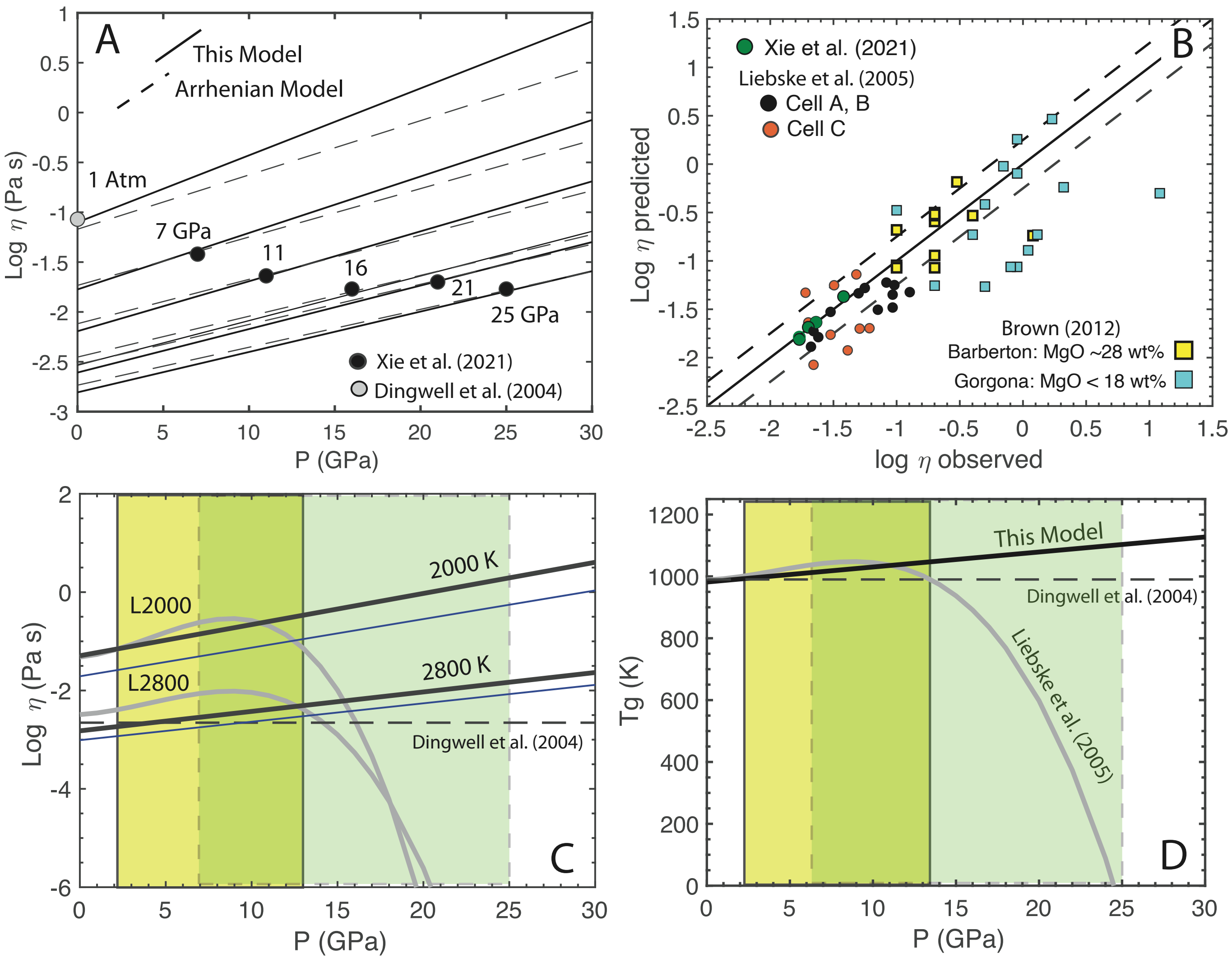

Figure 6. Ultamafic melt viscosity, 2024

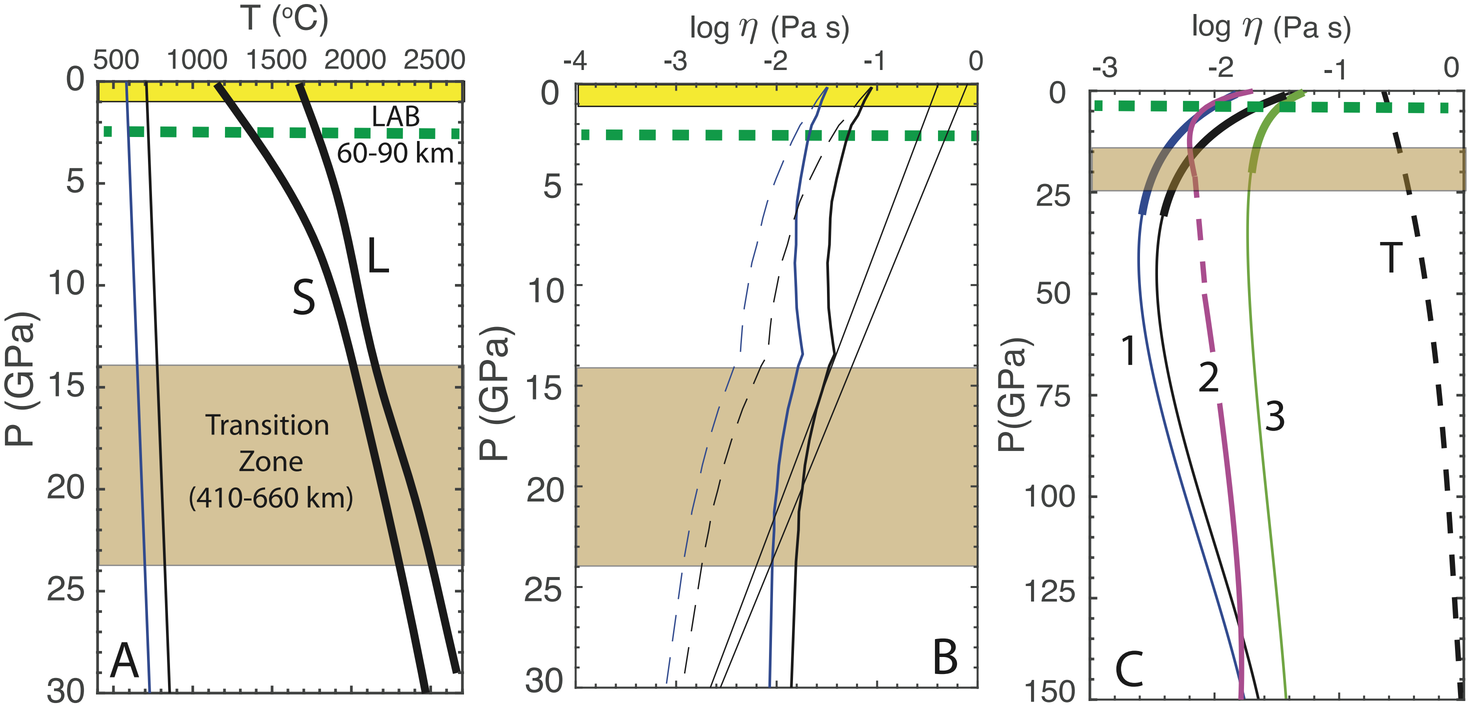

Figure 7. Ultramafic melt viscosity, 2024

Table S1. Compositions of peridotite, pyrolite and related melts used for measurements of melt viscosity.

	Dingwell et al. (2004)	Casas et al. (2023; Samples BAPYR-)							DiGenova et al. (2023)												Xie et al.
Sample	Peridotite	Pyrolite	19-LMU1	211-LMU07-09	211-LMU10-12	211-LMU13-15	19-LMU6	211-LMU16-19	S44F0	S44F6+	S44F6	S44F12+	S44F12	S40F6	S45F7	S34F0	S38F5W1	S40F5W6	S43F7W8	S39F6W12	Peridotite
Method[1]	CC & DSC	CC	MP	MP	MP	MP	MP	MP	MP & DSC	MP & DSC	MP & DSC	MP & DSC	MP & DSC	DSC	DSC	DSC	FDSC	FDSC	FDSC	FDSC	FSV
SiO_2	45.83	46.89	46.73	46.02	45.52	46.39	46.87	45.73	50.80	48.56	48.11	46.41	46.50	46.57	51.30	39.99	44.49	45.25	46.58	42.97	46.60
TiO_2	0.18	-	-	-	-	-	-	-	0.03	0.01	0.01	0.03	0.03	0.02	0.02	0.02	0.20	0.21	0.32	0.14	-
Cr_2O_3	0.36	-	-	-	-	-	-	-	0.00	0.00	0.00	0.00	0.00	0.00	0.00	0.00	0.21	0.21	0.24	0.19	-
Al_2O_3	4.87	4.31	4.31	4.03	3.92	4.09	4.32	4.11	6.62	6.36	6.47	6.14	6.01	4.05	4.12	4.09	3.18	3.78	4.61	3.00	4.00
FeO(T)	8.63	8.71	8.62	8.83	8.99	8.68	8.70	8.33	0.07	8.23	8.51	15.58	15.82	8.83	9.00	0.07	7.57	6.26	8.73	7.40	8.70
MnO	-	-	-	-	-	-	-	-	0.01	0.01	0.01	0.01	0.03	0.01	0.01	0.00	0.15	0.13	0.17	0.09	-
MgO	31.63	37.91	37.91	38.45	38.88	38.32	37.88	39.31	35.25	29.87	30.07	25.02	24.96	36.94	32.31	38.98	40.70	38.95	31.86	39.61	37.10
CaO	6.37	2.16	2.14	2.37	2.41	2.41	2.15	2.43	7.13	6.88	6.73	6.73	6.58	3.52	3.16	16.82	3.01	2.92	4.25	2.00	3.60
Na_2O	0.32	-	-	-	-	-	-	-	0.02	0.03	0.02	0.00	0.02	0.02	0.01	0.01	0.21	0.23	0.28	0.16	-
K_2O	0.00	-	-	-	-	-	-	-	0.02	0.03	0.03	0.03	0.03	0.02	0.04	0.00	0.04	0.06	0.06	0.02	-
P_2O_5	-	-	-	-	-	-	-	-	0.05	0.00	0.03	0.05	0.03	0.03	0.03	0.03	0.00	0.00	0.00	0.00	-
H_2O	-	-	-	-	-	-	-	-	-	-	-	-	-	-	-	-	0.23	2.00	2.90	4.44	-
Total	98.19	99.98	99.71	99.70	99.72	99.89	99.92	99.91	100	100	100	100	100	100	100	100	100	100	100	100	100.00
$Fe^{3+}/\Sigma Fe$	-	-	0.29	0.27	0.25	0.09	0.06	0.07	0.00	0.54	0.50	0.38	0.31	0.32	0.34	0.00	0.00	0.00	0.00	0.00	-
Fe_2O_3	-	-	2.82	2.67	2.54	0.92	0.64	0.61	0.00	4.94	4.73	6.58	5.45	3.14	3.40	0.00	0.00	0.00	0.00	0.00	-
Mg No.	86.7	88.6	88.7	88.6	88.5	88.7	88.6	89.4	99.9	86.6	86.3	74.1	73.8	88.2	86.5	99.9	90.5	91.7	86.7	90.5	88.4
NBO/T	2.27	2.45	2.45	2.56	2.62	2.52	2.44	2.60	1.93	1.97	1.99	2.01	2.02	2.49	2.02	3.30	2.87	2.86	2.56	3.46	2.50
SM	52.5	54.1	54.1	55.0	55.5	54.7	54.1	55.6	52.4	49.8	50.1	47.4	47.3	54.3	49.1	64.2	57.2	53.0	47.2	50.7	54.4

[1] Measurement techniques include: concentric cylinder viscometry (CC), micro-penetration (MP), conventional differential scanning calorimetry (DSC), flash differential scanning calorimetry (FDSC), and falling sphere viscometry (FSV).

Table S2. Compilation of all experimental data, and their sources, used to calibrate the temperature-dependent model for anhydrous and hydrous ultramafic melts.

Source	Composition	Label	Method[1]	T(°C)	log η (Pa s)	σ
Dingwell et al. (2004)	Peridotitic	OPL1	CC	1593.79	-0.96657	0.08
		OPL2	CC	1583.95	-0.9431	0.08
		OPL3	CC	1574.10	-0.8996	0.08
		OPL4	DSC	732.9	10.73	0.25
		OPL5	DSC	739.9	10.52	0.25
		OPL6	DSC	739.9	10.43	0.25
		OPL7	DSC	743.9	10.25	0.25
		OPL8	DSC	744.9	10.13	0.25
Casas et al. (2023)	Pyrolite (in Air)	BAPYR	CC	1664.0	-1.07	0.08
		BAPYR	CC	1654.0	-1.06	0.08
		BAPYR	CC	1644.0	-1.05	0.08
		BAPYR	CC	1634.0	-1.03	0.08
		BAPYR	CC	1624.0	-1.01	0.08
		BAPYR	CC	1614.0	-0.99	0.08
	Pyrolite (reduced fO_2)	19-LMU1	DSC	740.0	10.43	0.08
		211-LMU07-09	DSC	743.0	10.43	0.08
		211-LMU10-12	DSC	742.0	10.43	0.08
		211-LMU13-15	DSC	745.0	10.43	0.08
		19-LMU6	DSC	744.0	10.43	0.08
		211-LMU16-19	DSC	748.0	10.43	0.08
DiGenova et al. 2023	Peridotite (Fe-free)	S44F0	MP	750.9	11.20	0.15
		S44F0	MP	765.9	10.35	0.15
		S44F0	MP	756.9	10.85	0.15
		S44F0	DSC	740.9	11.79	0.15
		S44F0	DSC	745.9	11.49	0.15
		S44F0	DSC	764.9	10.43	0.15
		S44F0	DSC	772.9	10.13	0.15
	Peridotite (in Air)	S44F6	MP	710.9	11.36	0.15
		S44F6	MP	727.9	10.50	0.15
		S44F6	DSC	700.9	11.79	0.15
		S44F6	DSC	708.9	11.49	0.15
		S44F6	DSC	728.9	10.43	0.15
		S44F6	DSC	735.9	10.13	0.15
		S44F12	MP	678.9	11.52	0.15
		S44F12	MP	695.9	10.41	0.15
		S44F12	DSC	668.9	11.79	0.15
		S44F12	DSC	676.9	11.49	0.15
		S44F12	DSC	695.9	10.43	0.15
		S44F12	DSC	703.9	10.13	0.15
		S40F6	DSC	716.9	11.79	0.15
		S40F6	DSC	737.9	10.43	0.15
		S45F7	DSC	711.9	11.79	0.15
		S45F7	DSC	736.9	10.43	0.15
		S44F6+	MP	712.9	11.36	0.15
		S44F6+	DSC	702.9	11.79	0.15
		S44F6+	DSC	709.9	11.49	0.15
		S44F6+	DSC	729.9	10.43	0.15
		S44F6+	DSC	736.9	10.13	0.15

	Peridotite (Oxidized)	S44F12+	MP	683.9	11.40	0.15
		S44F12+	MP	701.9	10.52	0.15
		S44F12+	DSC	673.9	11.79	0.15
		S44F12+	DSC	682.9	11.49	0.15
		S44F12+	DSC	701.9	10.43	0.15
		S44F12+	DSC	710.9	10.13	0.15
	Peridotite (Fe-free/ High Ca)	S34F0	DSC	755.9	11.79	0.15
	Peridotite (Fe-free)	S34F0	DSC	776.9	10.43	0.15
	Peridotite (Hydrous)	S38F5W1-0.65	FDSC	781.9	8.01	0.15
		S38F5W1-0.65	FDSC	816.9	6.65	0.15
		S40F5W6-5.51	FDSC	664.9	8.01	0.15
		S40F5W6-5.51	FDSC	733.9	6.65	0.15
		S43F7W8-8.13	FDSC	622.9	8.01	0.15
		S43F7W8-8.13	FDSC	686.9	6.65	0.15
		S39F6W12-11.62	FDSC	605.9	8.01	0.15
Xie t al. (2021)	Peridotite (High-P)	S3301-7GPa	FSV	1900	-1.420	0.05
		S3296-11GPa	FSV	2097	-1.638	0.05
		S3298-16GPa	FSV	2300	-1.770	0.05
		S3299-21GPa	FSV	2350	-1.699	0.05
		S3376-25GPa	FSV	2500	-1.770	0.05

[1] Measurement techniques include: concentric cylinder viscometry (CC), micro-penetration (MP), conventional differential scanning calorimetry (DSC), flash differential scanning calorimetry (FDSC), and falling sphere viscometry (FSV).

Table S3. Example calculation of VFT parameters for predicting *T*-dependent melt viscosity [$\log_{10} \eta = A + B/(T(K) - C)$] for a hydrous peridotitic melt at elevated pressure.

$$\log \eta = A + [b_0 + b_1 \ (P\text{-}0.0001)] \ / \ [T - (c_0 + c_1 \ Mg\# + c_2 \ X_{H2O}^{0.5}) \ ]$$

Parameters	**Values**	**Oxide**	**Wt %**	**Mol %**	**X_{H2O}**
A	-5.4	SiO_2	45.83	40.32	0.029
		TiO_2	0.18	0.12	**Mg#**
b_0	5558.3	Al_2O_3	4.87	2.52	86.7
b_1	77.5	FeO(T)	8.63	6.35	**B Term**
c_0	422.93	MnO	0.00	0.00	5752.0
c_1	2.69	MgO	31.63	41.48	**C Term**
c_2	-589.39	CaO	6.37	6.00	555.3
		Na_2O	0.32	0.27	**Tg K (~10^{12} Pa s)**
P(GPa)	2.5	K_2O	0.00	0.00	886
		H_2O	1.00	2.93	**Fragility (*m*)**
		Total	98.83	100.00	46.6

Supplement 4: Other models for multicomponent melt viscosity.

Other models for predicting multicomponent silicate melt viscosity at geological conditions do not accurately reproduce the experimental data for ultramafic viscosity melts. The model of Shaw (1972) does best at high-T where ultramafic melts are most Arrhenian-like but fails to reproduce the low-temperature data (anhydrous and hydrous) (Fig. 1A). The multicomponent non-Arrhenian models (Hui and Zhang, 2007; Giordano et al 2008) reproduce the experimental data better on average but do not account for pressure. They also reproduce the high-temperature data better than the low-T data.

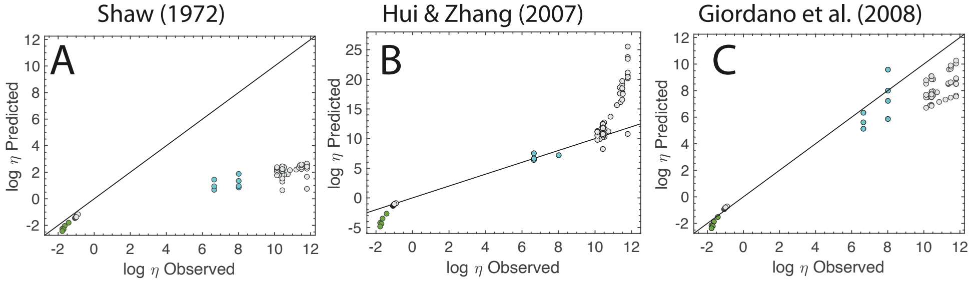

Figure 1. Comparison of measured values of viscosity for ultramafic melts (See Tables S1 & S2) to values predicted by: (A) Arrhenian melt model of Shaw (1972); and non-Arrhenian models of (B) Hui and Zhang (2007) and (C) Giordano et al. (2008). Symbols denote anhydrous (Grey), hydrous (blue) and high-P melts (as in Fig. 1 in text).

There are two multicomponent Arrhenian models that do account for pressure. Neither reproduces the high-pressure data well even at high-T (Fig. 2). The Duan (2014) model underestimates the viscosity of high-T melts at elevated P and overshoots the viscosity of 1-atm, high-T melts. Because the model is Arrhenian, it undershoots the low-T anhydrous and hydrous data (Fig. 2A). The model of Persikov and Bukhtiyarov (2009) accounts for pressure but overshoots the high-P melt viscosity data (Fig. 2B).

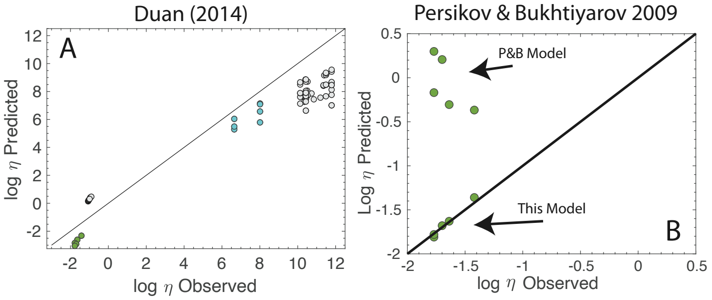

Figure 2. Comparison of measured values of viscosity for ultramafic melts to values predicted by: (A) Arrhenian P-dependent viscosity model of Duan (2014); symbols as in Fig. 1. (B) Comparison of high-P viscosity data (Xie et al. 2021) to values predicted by Persikov and Bukhtiyarov (2009) and the model presented here.

Reference

Duan X (2014) A model for calculating the viscosity of natural iron-bearing silicate melts over a wide range of temperatures, pressures, oxygen fugacites, and compositions. Am Mineral 99:2378–2388

Hui H, Zhang Y (2007) Toward a general viscosity equation for natural anhydrous and hydrous silicate melts. Geochim Cosmochim Acta 71:403–416

Giordano, D., Russell, J.K., Dingwell, D.B., 2008. Viscosity of magmatic liquids: a model. Earth Planet. Sci. Lett. 271, 123–134. https://doi.org/10.1016/j.epsl.2008.03.038.

Persikov ES, Bukhtiyarov PG (2009) Interrelated structural chemical model to predict and calculate viscosity of magmatic melts and water diffusion in a wide range of compositions and *T-P* parameters of the Earth's crust and upper mantle. Russ Geol Geophys 50:1079-1090

Shaw HR (1972) Viscosities of magmatic silicate liquids; an empirical method of prediction. Am J Sci 272, 870–893

Xie L, Yoneda A, Katsura T, Andrault D, Tange Y, & Higo Y (2021). Direct viscosity measurement of peridotite melt to lower-mantle conditions: A further support for a fractional magma-ocean solidification at the top of the lower mantle. Geophys. Res. Lett. 48, e2021GL094507. https://doi. org/10.1029/2021GL094507

Supplement 5: Analysis of Covariance.

The form of the VFT function is non-linear with respect to the unknown parameters (Eq. 1; *A*, *B* and *C*; see text) and is solved by conventional iterative methods (e.g., Press et al. 1986). One attribute of using the χ2 merit function is that, rather than considering a single solution that coincides with the minimum residuals, we can map a solution region at a specific confidence level (e.g., 1σ; Press et al. 1986). This allows delineation of the full range of parameter values that can be considered equally valid descriptors of the experimental data at the specified confidence level (e.g., Russell et al. 2002). Furthermore, the confidence limits accurately portray the magnitude and nature of covariances between model parameters.

Russell et al. (2002, 2003) showed that the nonlinear character of non-Arrhenian models ensures strong numerical correlations between, and even nonunique estimates of, model parameters. One result of the strong covariances between model parameters is that wide ranges of values can be used to describe individual datasets. This is true even where the data are numerous, well-measured and span a wide range of temperatures and viscosities. Stated another way, there is a substantial range of model values which, when combined in a nonarbitrary way, can accurately reproduce the experimental data.

In our model for the temperature, pressure and compositional dependence of viscosity for ultramafic melts we have adopted an independently fixed value for *A* (-5.4; see text), representing the high-temperature limit to melt viscosity. Our optimization for the values of the 5 adjustable parameters (b_0, b_1, c_0, c_1, c_2) was based on minimization of the χ2 function (Eq. 4; see text). These parameters have optimal values and statistical uncertainties reflecting the quality and distribution of the data. The parameters also have covariances which dictate the non-arbitrary way in which the permitted range of parameter values can be combined to reproduce the original data.

In Figure 1, we illustrate these concepts explicitly by displaying the covariances between several of the parameters for which there are significant covariances (Table 1; see text). The 1σ confidence envelopes on the optimal 5 parameter solutions define 5-D ellipsoids. The 2-D ellipses plotted in Fig. 1 approximate those confidence envelopes on two parameters where the other parameters are fixed at their optimal values. These ellipses are planes through the 5-D ellipsoid that contain the solution and are normal to the fixed parameter space. The confidence envelopes are computed by mapping boundaries of constant χ2 around the optimal solution in the manner described fully by Press et al. (1986). The methods used to compute the confidence ellipses and applied to models for melt viscosity are fully described in Russell et al. (2002), and Giordano et al. (2015).

Firstly, all parameters have variances that are significantly less than their optimal value and, thus, do not allow for a zero value. This means that each parameter is statistically relevant to the model used to capture the data. Two parameter pairs show weak negative covariation, c_0 vs. b_0 and b_0 vs. $b_1$and one pair shows a weak positive correlation (c_0 vs. c_2). The parameters c_2 and b_1 show no pronounced covariation. Overall the covariations between model parameters are weak implying that they are more or less independent

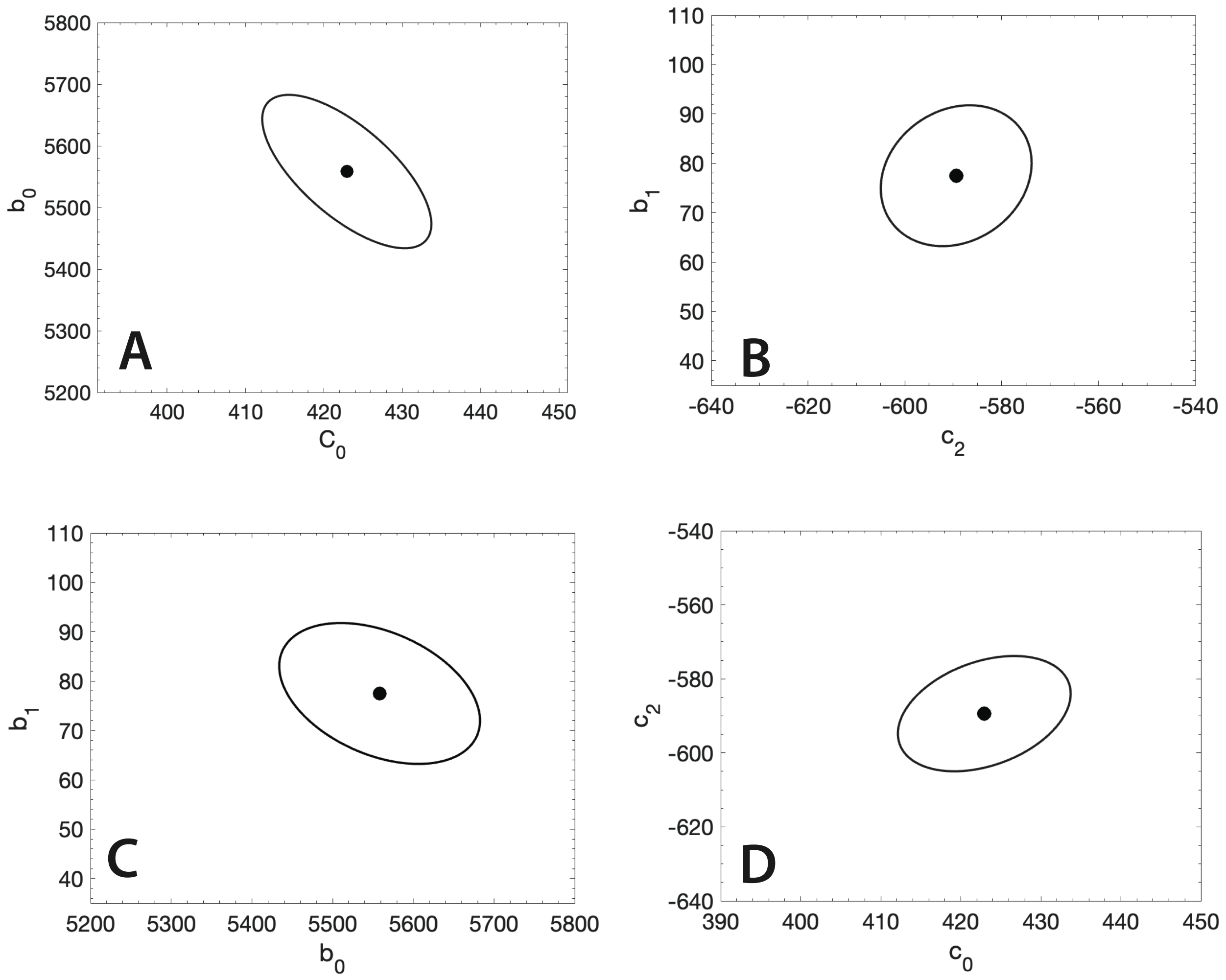

Figure 1. The two-dimensional projected 1σ confidence ellipses (solid lines) centered on the optimal solution for the adjustable parameters b_0, b_1, c_0, c_1, c_2. Confidence ellipses are drawn for pairs of parameters where the other three parameters are held constant at their optimal values. The plots show the magnitude and nature of correlation between: (A) c_0 and b_0, (B) c_2 and b_1, (C) b_0 and b_1, and (D) c_0 and c_2. The axes in each diagram are scaled to ~3 standard deviations for each parameter to compare the relative magnitudes of covariance.

Reference

Giordano, D., Nichols, A.R.L., Potuzak, M., Di Genova, D., Romano, C., Russell, J.K. (2015) Heat capacity of hydrous trachybasalt from Mt Etna: comparison with $CaAl_2Si_2O_8$ – $CaMgSi_2O_6$ as basaltic proxy compositions. Contrib. Mineral. Petrol. 70, 48.

Press WH, Flannery BP, Teukolsky SA, Vetterling WT (1986) Numerical recipes: the art of scientific computing. Cambridge University Press, Cambridge

Russell JK, Giordano D, Dingwell DB, Hess KU (2002) Modelling the non-Arrhenian rheology of silicate melts: numerical considerations. Eur. J. Mineral. 14, 417–427.

Russell JK, Giordano D, Dingwell DB (2003) High-temperature limits of non-Arrhenian silicate melts: implications for modelling compositional dependencies. Am. Mineral. 88, 1390–1394.